This paper is the accepted version of the paper published on IEEE Transactions On Geoscience And Remote Sensing, VOL. 53, NO. 1, JANUARY 2015

Digital Object Identifier 10.1109/TGRS.2014.2319265

Radiometric Approach for Estimating Relative Changes in Intra-Glacier Average Temperature

Kenneth C. Jezek[1], Joel T. Johnson[2], Mark R. Drinkwater[3], Giovanni Macelloni[4], Leung Tsang[5], Mustafa Aksoy[2], and M. Durand[1]

1. 1090 Carmack Road, Byrd Polar Research Center, The Ohio State University, Columbus OH 43210

2. Department of Electrical and Computer Engineering, The Ohio State University

3. European Space Agency, Noordwijk, The Netherlands

4. Institute of Applied Physics, Florence, Italy

5. Department of Electrical Engineering, University of Washington

Abstract

We investigate the degree to which ultra high frequency (UHF) radio emission can be used to estimate subsurface physical temperature in the polar ice sheets. We combine electromagnetic-emission forward-models with plausible models of depth-dependent physical properties in the ice sheet. Temperature models are parameterized with variables including accumulation rate, geothermal heat flux and surface temperature. Scattering is parameterized using empirical observations of grain growth combined with measured densities. Electromagnetic absorption is modeled using dielectric dispersion processes and semi-empirical models based on observations. Our models illustrate that information about East Antarctic ice sheet temperature from near the surface to near the base can be gleaned from ultra-wideband radiometer data. Based on our modeling study we illustrate an instrument-concept to measure ice-sheet temperature-profiles comprising a novel, ultra-wide-band radiometer.

1.0 Introduction

Spaceborne and airborne remote sensing instruments characterize most of the important variables necessary to understand current ice sheet behavior, and to predict future changes in ice sheet volume and mass. Derived geophysical quantities include: ice sheet surface topography; ice surface velocity; ice sheet surface elevation change; mass change; ice sheet thickness; surface accumulation rate; internal layer stratigraphy; seaward bathymetry; and basal geology [1]. At present, internal ice sheet temperature is absent from this list, yet temperature is a primary factor in determining the ease at which ice deforms internally and also the rate at which the ice flows across the base. Consequently, ice temperature is fundamental for better understanding changes in ice sheet mass balance and dynamics.

Temperature enters as a variable in glacier dynamics through a flow law typically taken as a power law relation between stress and strain rate [2, 3]. The flow rate is determined by the strain rate ($\dot{\epsilon}_{ij}$, per year) and deviatoric stress (σ'_{ij} , bar) relationship as follows:

$$\sigma'_{ij} = B\dot{\epsilon}_e^{\frac{1}{n}-1}\dot{\epsilon}_{ij} \quad (1)$$

where the effective strain is

$$\dot{\epsilon}_e^2 = \frac{1}{2}\dot{\epsilon}_{ij}\dot{\epsilon}_{ij} \quad (2)$$

for which i and j represent the three orthogonal coordinates, *n* is a parameter taken to be about 3, and B is a stiffness parameter which is highly temperature dependent (Figure 1 left) [4]. Because ice sheet temperature varies with depth (figure 1 center), the stiffness parameter and hence strain rates vary with depth (figure 1 right). Temperature at depth is therefore key information for modeling ice sheet flow (see for example [5]).

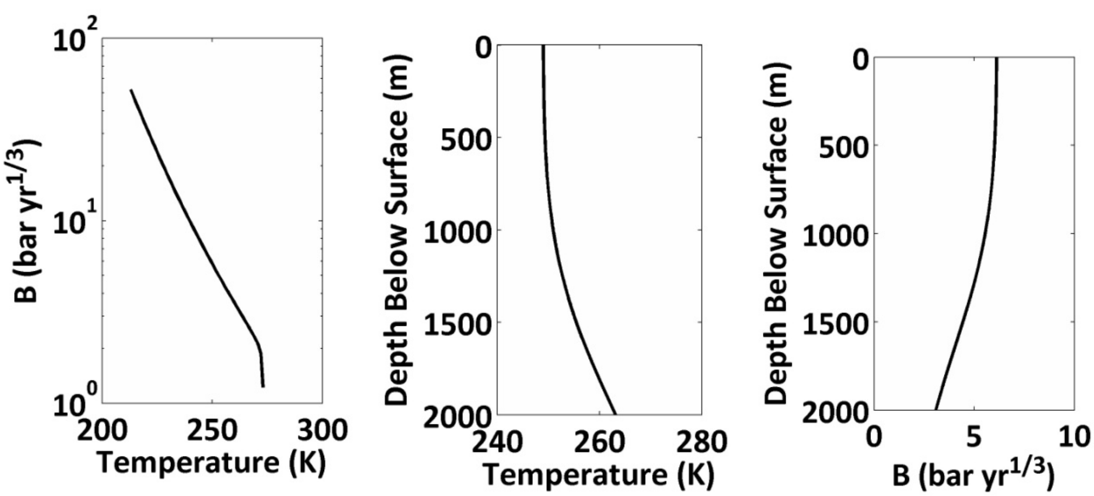

Figure 1. Variation of the ice stiffness parameter B with temperature in degrees centigrade (left). A simple model of depth-varying ice-sheet temperature in degrees Kelvin (center). Variation of B with depth in the ice sheet (right) using results presented in the left and center frames.

Presently, the only information about ice sheet internal temperature arises from the small number of boreholes in which temperatures are directly measured and from modeling. Here, we investigate the degree to which UHF radiometry (300 MHz to 3 GHz) can provide clues to relative changes in average ice-sheet internal temperatures. We use plausible models of depth-varying ice sheet temperatures, physical properties and electromagnetic loss to model emission and brightness temperature at the ice sheet surface. We use our modeling results to develop an instrument-concept for an ultra wide band radiometer capable of probing the internal temperature of the ice sheet.

2.0 Brightness Temperature Model

In this section, we describe a UHF brightness temperature model driven by plausible models of ice sheet physical properties. First the physical properties are chosen to be representative of the interior East Antarctic Ice Sheet. Subsequently we vary ice-sheet physical-property parameters to investigate brightness temperature sensitivities at several frequencies.

2.1 Temperature Model

We adopt the Robin temperature model as described in [5] and vary accumulation rate (M) measured in m/yr ice equivalent. This model assumes a planar stratified medium with homogenous thermal parameters that is driven by geothermal heat flux alone. These are significant assumptions, but sufficient for the purposes of the current initial study, where the purpose is to produce realistic temperature profiles as a basis for assessing the impact on the frequency-dependent brightness temperature. Ignoring lateral sensible heat advection, the temperature profile (T(z)) is given as

$$T(z) = T_s - \frac{G\sqrt{\pi}}{2k_c\sqrt{\frac{M}{2k_d H}}}\left(\operatorname{erf}\left(z\sqrt{\frac{M}{2k_d H}}\right) - \operatorname{erf}\left(H\sqrt{\frac{M}{2k_d H}}\right)\right) \quad (3)$$

Here, erf is the error function, G is the geothermal heat flux (47 mW/m^2), Ts is the surface temperature (which is held constant at 216 K throughout what follows), k_c is the ice thermal conductivity (2.7 W m^{-1} K^{-1}), k_d is the ice thermal diffusivity (45 m^2 yr^{-1}), H is the ice thickness (set to 3700 m), M is the accumulation rate in m/yr, and z is the elevation variable.

Parameters were chosen to yield several realistic temperature profiles (Figure 2) comparable to temperature-depth profiles measured in East Antarctica [6, 7, 8]. The accumulation rate in Figure 2 varies from a low value of 0.01 m/yr and increases in 0.01 m/yr increments. The average temperature at depth decreases as the accumulation rate increases. At the lowest accumulation rate of 0.01m/y, and given a mean annual surface temperature of 216 K [8] the temperature at the base of the ice sheet (~3700m depth at Lake Vostok) approaches the melting point for this model.

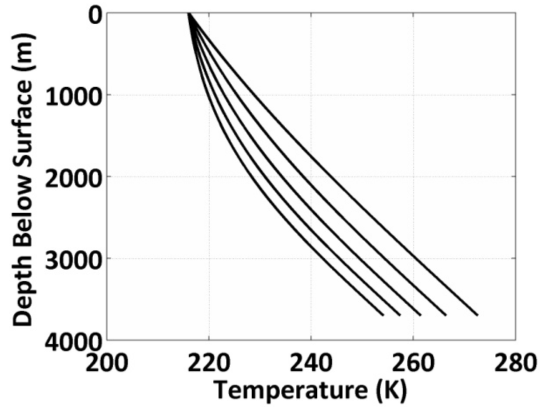

Figure 2. Modeled temperature profile for different values of accumulation rate to 3700 m depth. The rightmost (warmest profile) is calculated using the lowest accumulation rate of 0.01 m/yr , whilst the 5 curves represent accumulation rates of 0.02, 0.03, 0.04 and 0.05 m/y (from right to left), respectively.

2.2 Electromagnetic Loss Model

Predicting the electromagnetic propagation and observed brightness temperature requires a description of the electromagnetic loss as a UHF signal propagates through a small distance in the ice sheet; this loss can vary as a function of ice temperature and therefore depth. In this section, we discuss loss estimated using a Debye model which provides insight into low frequency behavior (500 MHz or less for our purposes) and specific physical mechanisms [9]. Discussion of the Debye model is useful for illustrating the physical loss-mechanisms at the lower end of our band of interest. However loss estimated with the Debye model is insensitive to frequency changes for most of the band we are interested in. For higher frequencies, and for all of our subsequent brightness temperature modeling, we adopt the semi-empirical model for complex permittivity described by Mätzler [10]. The Mätzler model better captures higher frequency attenuation associated with an additional dispersion process. More importantly, inclusion of an additional dispersion mechanism reintroduces a strong, frequency-dependent loss in the microwave region.

The Debye dielectric dispersion with the addition of a free charge conductivity to compute radio frequency loss through the ice is given as (e.g. eq. (2) from Von Hippel [11]):

$$\varepsilon'' = \frac{\sigma_f}{\omega\varepsilon_0} + \sum_n \frac{\omega\Delta\varepsilon_n\tau_n}{1+\omega^2\tau_n^2} \quad (4)$$

Here ε'' is the lossy part of the effective complex dielectric constant, ω is the frequency, σ_f is the free charge conductivity, ε_0 is the permittivity of free space, τ_n is the relaxation time for the nth dispersion, and $\Delta\varepsilon_n$ is the difference between the real parts of the high and low frequency dielectric constants. In this initial discussion, we consider only a single, low-frequency dispersion (loss peak at about 100 kHz). Under these assumptions and in the high frequency limit (product of the angular frequency and the relaxation time (τ) is much greater than unity), the absorption coefficient (in Nepers/m) becomes

$$\kappa_a = \frac{k_0}{\sqrt{\varepsilon'}}\varepsilon'' \cong \frac{1}{c\sqrt{\varepsilon'}}\frac{\Delta\varepsilon}{\tau} + \frac{\sigma_f}{c\varepsilon_0\sqrt{\varepsilon'}} \quad (5)$$

Here $\Delta\varepsilon$ is the difference between the low (taken here to be 100) and high (taken to be 3.17 and represented as ε' in the equation) frequency real parts of the permittivity of ice. We choose a free charge conductivity of 10^{-7} S/m which corresponds to pure ice at 263 K and is associated with proton migration through the ice lattice [12]. The combined dielectric and conductive losses result in an equivalent conductivity of about 10^{-5} S/m. Values for $\Delta\varepsilon$, σ_f, and ε are initially assumed temperature independent in this analysis because the values are only slightly varying as compared to the temperature variation in the relaxation time (τ). Temperature variations in τ are included through

$$\tau = Ce^{\frac{E_\tau}{kT}} \quad (6)$$

In equation (6), C is estimated to be $6.45*10^{-16}$ s (extrapolated from data in Hobbs [13, p. 92]), E_τ is the activation energy (0.51 eV), k is Boltzman's constant, and T is temperature expressed in Kelvins. The temperature dependence of τ therefore results in a depth dependence for the electromagnetic attenuation.

Using the temperature profiles in Figure 2, and equation (6), Figure 3 illustrates the resulting specific attenuation (loss in dB per 100 m) versus depth in the ice sheet. The results indicate a loss rate which in general increases with depth but decreases with sequentially increasing accumulation rate. The rightmost curve with largest absorption loss corresponds to the lowest accumulation rate of 0.01 m/yr. As the accumulation rate is increased, downwardly advected cold-ice cools the temperature profile and the loss decreases correspondingly.

For the warmest temperature profile and lowest accumulation rate, our model predicts results similar to MacGregor and others' [14] radio-frequency absorption-model based on the measured Vostok ice core chemistry and modeled borehole temperature.

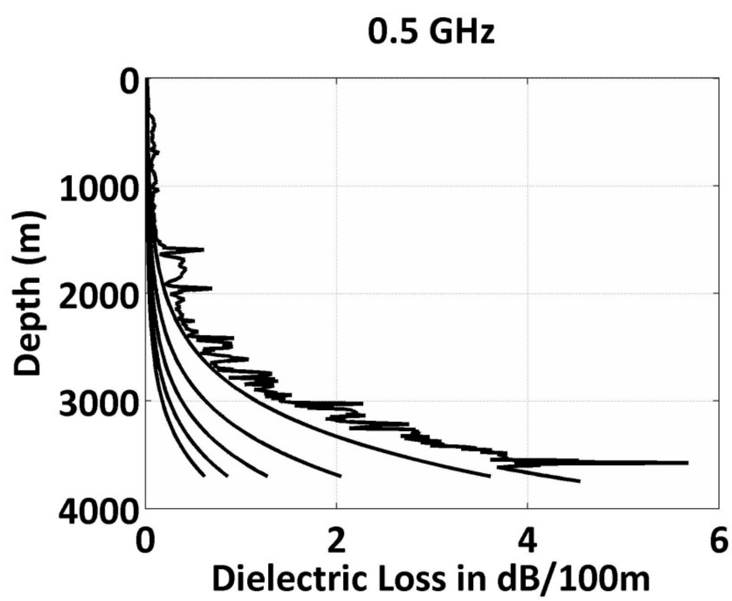

Figure 3. Ice specific attenuation using the Debye model and temperatures (smooth curves) which vary with accumulation rate (warmer profiles have higher loss) from Fig 2. Specific attenuation is independent of frequency for this dispersion model. For comparison, the irregular line shows MacGregor and others [14] modeled absorption values. The curve with largest absorption loss corresponds to the least accumulation rate (0.01 m/yr). As the accumulation rate is increased, downwardly advected cold-ice cools the temperature profile and the loss is decreased.

To show how the different loss processes contribute to the total absorption loss, we plot the ratio of the conductive and equivalent dielectric conductivity terms from Equation 5 in Figure 4. Near the surface where temperatures are cold and the loss is low, the free charge conduction term dominates. As the temperature warms with depth and where the loss is high, the dielectric term dominates. The implication is that small changes in the free charge conductivity will not have an important impact on the total loss at low frequencies.

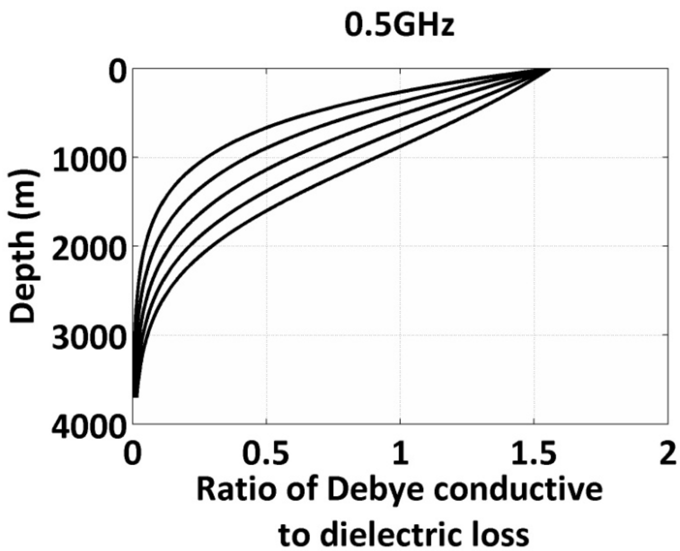

Figure 4. Ratio of conductive and dielectric loss terms contributing to the absorption coefficient of Equation 5. The curves correspond to the different temperature models in Figure 2. The rightmost curve corresponds to the warmest temperature profile and lowest accumulation rate (0.01m/y). The family of curves corresponds with accumulation rate values of 0.01, 0.02, 0.03, 0.04 and 0.05 m/y from right to left. The left-most curve corresponds to the coldest temperature profile.

Because we are ultimately interested in using radiometry to derive information about temperature at depth and in view of practical technologies, we also investigate permittivity models at higher frequencies with additional dispersion terms. In particular, Mätzler [10] discusses the complex permittivity for ice for microwave radiation. Following Hufford [15], Mätzler models the imaginary part of the permittivity as the sum of two, temperature-dependent terms, one inversely proportional to frequency a second term proportional to frequency. The second term accounts for higher frequency dispersions neglected in our discussion of the Debye single dispersion model. The imaginary permittivity and loss from the Debye model with parameters described above and the Mätzler model are compared in Figure 5.

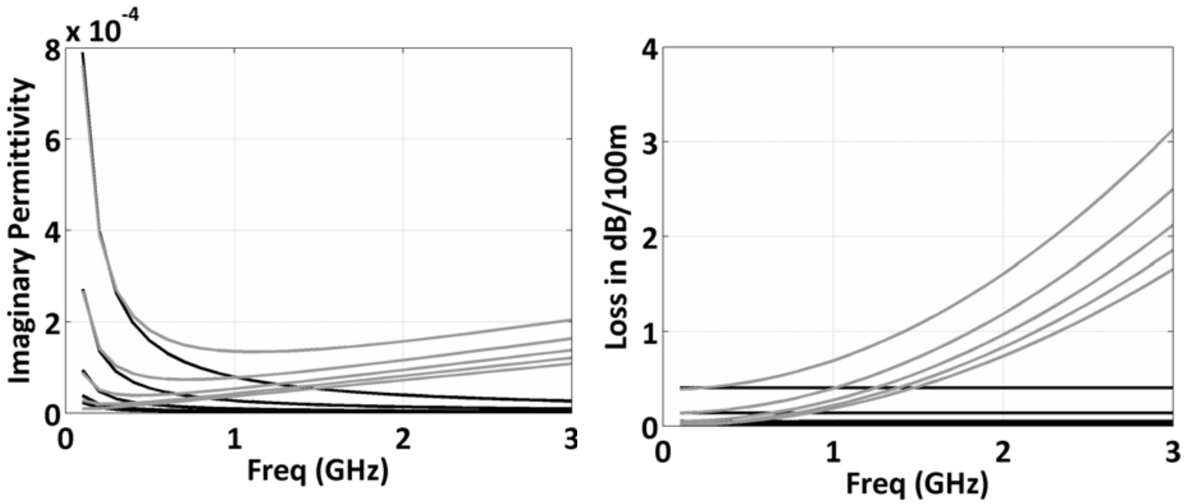

Figure 5. Debye (black) and Mätzler (gray) imaginary permittivity vs frequency(left) and loss vs frequency (right) for a set of curves representing 210, 220, 230, 240 and 250 Kelvin constant physical temperatures, respectively. Warmer temperatures correspond to sequentially higher imaginary permittivity and greater loss.

Notably, Figure 5 shows that the imaginary part of the complex permittivity exhibits a minimum in the Mätzler model between 0.5 and 1 GHz, depending on temperature. The Debye single dispersion model for loss is independent of frequency in this range whereas loss monotonically increases with frequency for the Mätzler model. The black and gray curves overlap at the lower frequencies where both models predict the same dielectric behavior.

Permittivities and loss at depth for the temperature models described above are shown for 3 different frequencies in Figures 6 and 7. The family of curves in each plot corresponds to the range of temperature profiles from the coldest profile (and highest accumulation) though to the warmest profile (and lowest accumulation. Figure 7 compares the loss curves generated using the Debye model (and shown in in Figure 3) with the Mätzler model. Importantly, the imaginary permittivity and loss are very similar for these two models at 0.5 GHz. But, for the two plots at frequencies above 0.5 GHz, the Mätzler model (grey curves) predicts greater loss at lower temperatures, and the modeled loss profiles are quite different, particularly in the colder ice in the upper portion of the temperature profiles. From this point onwards we use the Mätzler model to compute brightness temperatures described in the following sections.

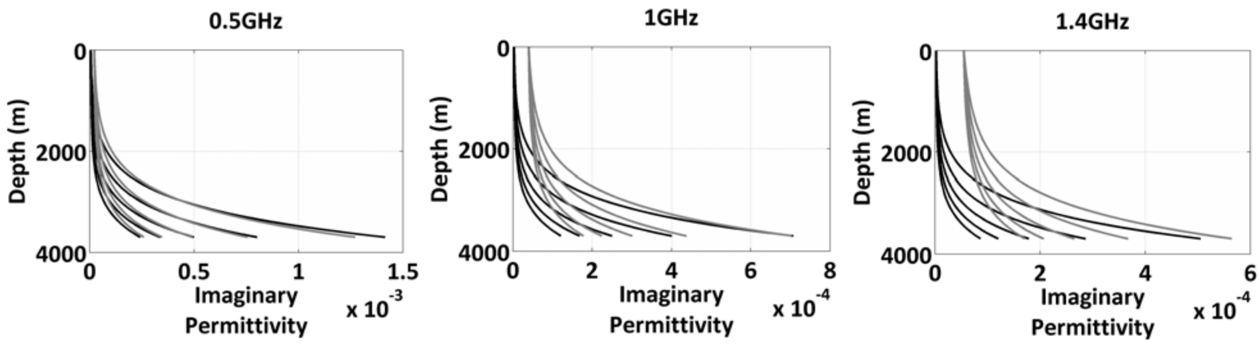

Figure 6. Imaginary permittivity with depth for the temperature profiles shown in Figure 2 using the Debye single dispersion model (in black) and the Mätzler model (in grey). The Mätzler model imaginary permittivity is larger than that of the Debye model for colder temperature and at higher frequencies.

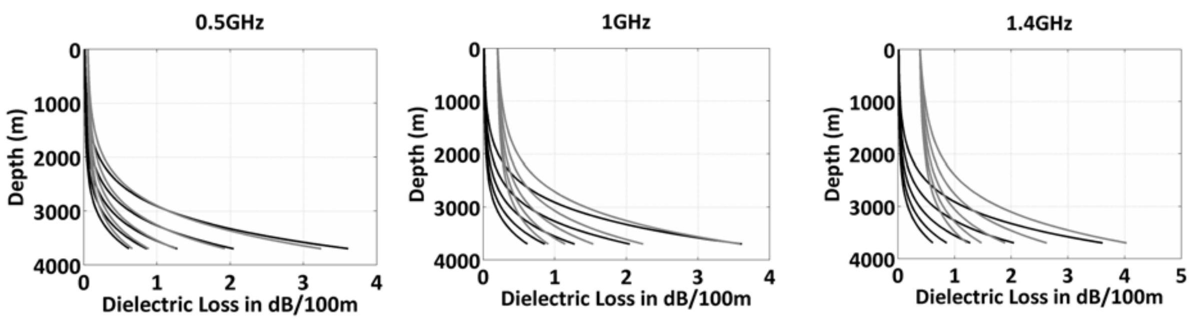

Figure 7. Dielectric loss in dB/100 m at depth for the temperature profiles in Figure 2 using the Debye single dispersion model (in black) and the Mätzler model (in grey). The Mätzler model predicts greater loss particularly at higher frequencies because of the inclusion of higher frequency dispersions.

2.3 Brightness Temperature Model

We discretely layer the ice sheet to compute local emission and also take into account the reflectivity at the surface (i.e. air/snow interface) and the base of the ice sheet (i.e. ice/rock or ice/water interface). For simplicity in what follows, the model is described for normal incidence (i.e. nadir) radiometric observations; the more complete formulation of [16] capable of addressing arbitrary observation angles and polarization effects was also implemented as a check. We assume the scattering coefficient (κ_s) is small compared to the absorption coefficient (κ_a). We take the physical temperature in the material beneath the glacier base to be constant and equal to the temperature of the bottom of the ice. We allow for either an isothermal, semiinfinite subglacial layer of frozen, rock-base or a liquid water-base depending on the basal temperature. Following Zwally [17], Swift and others [18], and van der Veen and Jezek [19] we represent the (normal incidence) calculation analytically as

$$T_B(z_s = 0) = \left(1 - R_{air/snow}\right)\left(\int_0^{z_s} (\kappa_a + \kappa_s) T e^{-\int_0^{z_s}(\kappa_a+\kappa_s)dz}\, dz + T_B(z = H) e^{-\int_0^{z_s}(\kappa_a+\kappa_s)dz}\right) \quad (7)$$

Here, $T_B(z_s=0)$ is the brightness temperature at the ice sheet surface that is observed by the radiometer, and $R_{air/snow}$ is the amplitude squared of the Fresnel reflection coefficient at the air snow boundary. $T_B(z_s=0)$ consists of the weighted integral of the emission from each depth plus the attenuated subglacial emission ($T_B(z=H)$) which under our assumption is simply the physical temperature multiplied by the amplitude squared of the Fresnel reflection coefficient at the ice sheet base. For oblique angles, the range terms in the equation are multiplied by the secant of the incidence angle. However because the critical angle for an air/ice boundary is about 33^o there will not be a strong angular dependence of brightness temperature due to changing path lengths through the ice.

We evaluated the integral by computing the emission at discrete layers within the ice and then summing the result. If the basal temperature approached 273^o K (allowing for pressure and likely impurities), we assumed a water surface at the basal boundary. Otherwise the basal material was assumed to be frozen rock with a physical temperature equal to that computed for the bottom of the ice.

Scattering is included by assuming a near surface distribution of Rayleigh scatterers. The grain size is estimated using Zwally's [17] fit to Gow's [20] parameterization of Plateau Station grain size (where a is the ice particle radius in mm) with depth (z)

$$a^3 = 0.0377 + 0.00472z \quad (8)$$

Using densities estimated from [21] (Figure 8), the particle density (Nd) is

$$Nd = \frac{\rho_{firn}}{\rho_{ice}} \frac{1}{\frac{4}{3}\pi a^3} \quad (9)$$

where ρ_{firn} is the density of the firn and ρ_{ice} is the density of ice.

Given the grain size and particle density (figure 8) from above, the Raleigh scattering coefficient (κ_s) is:

$$\kappa_s = Nd\frac{8\pi}{3}{k_0}^4 a^6 \left(\frac{\varepsilon_r - 1}{\varepsilon_r + 2}\right)^2 \quad (10)$$

The lower right panel in Figure 8 shows the scattering loss at 1.4 GHz estimated to 90 m depth. There is negligible scattering loss for this physical properties model at 500 MHz. We assume there is no scattering below 90 m depth due to the near-homogeneous ice composition at these depths.

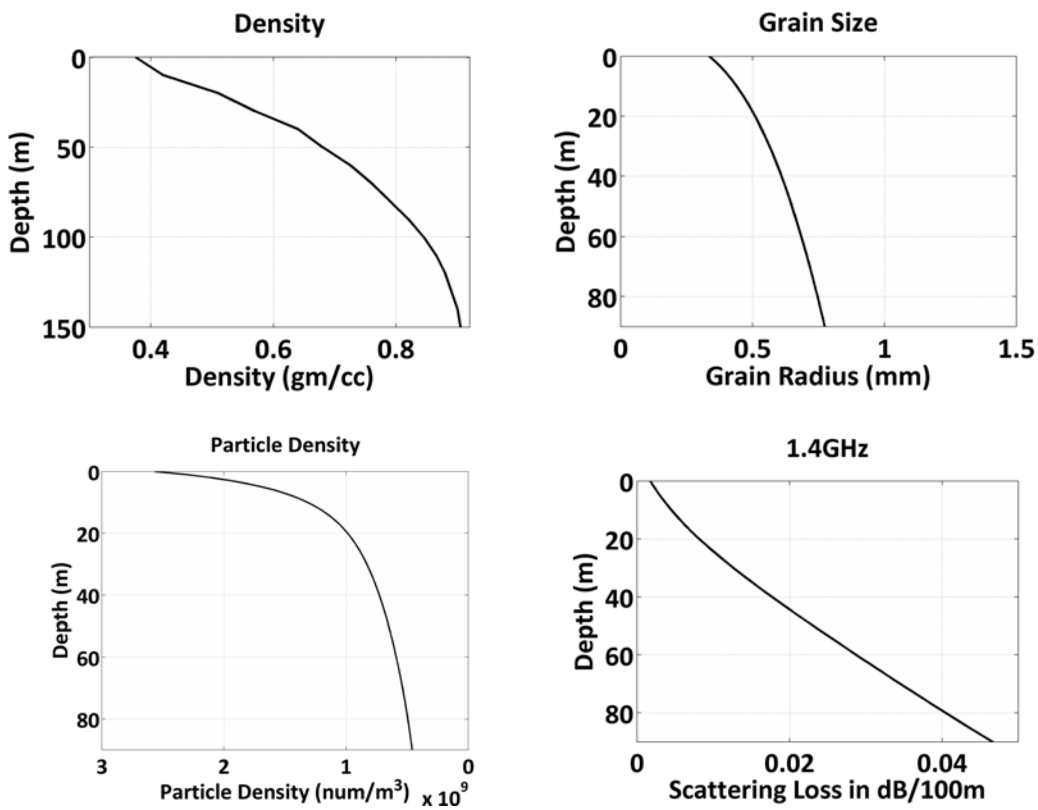

Figure 8. Ice-sheet, near-surface physical properties used to estimated scattering loss. Upper left panel is density at depth. Upper right is grain size estimated using the Gow [20] parameterization. Lower left is the particle density estimated using the density and grain size. Lower right is the scattering loss.

Figure 9 shows the cumulative brightness temperature for three different frequencies found by integrating the emission from successive layers down to a given layer of depth z. The integration proceeds from the surface to the base. At 0.5 GHz, and for only the warmest case does the brightness temperature approach a saturation value at the deepest part of the ice sheet. The result indicates that for this model, the entire ice sheet contributes to the surface brightness temperature. Contributions from the deepest layers are muted at frequencies above 1 GHz.

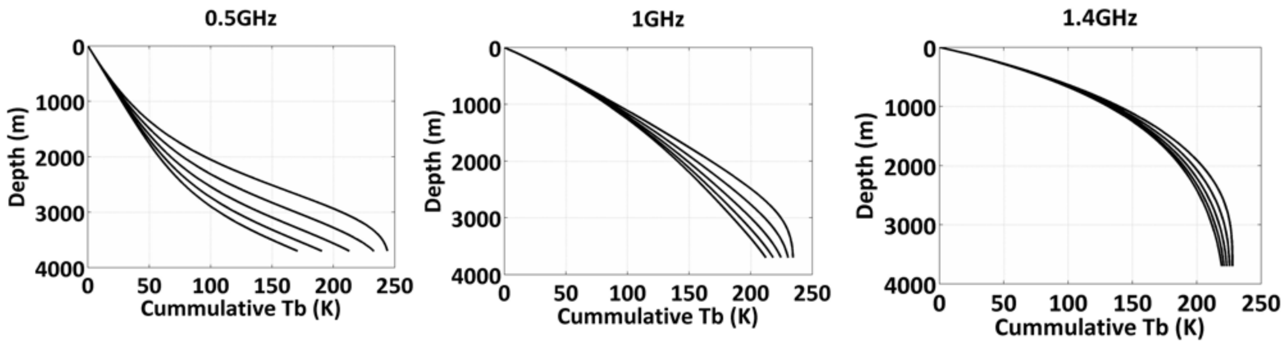

Figure 9. Cumulative brightness temperature found by summing emissions from the surface to each depth for the family of temperature profiles presented in Figure 2. Reflection loss at the surface is not included.

The results show that for this model all depths of the ice sheet contribute to the surface brightness temperature particularly for profiles exhibiting colder average physical temperatures. The brightness temperature begins to approach a warmer, saturation value at the higher frequencies and for the warmer, physical temperatures, owing to the greater losses in the deeper part of the vertical profile.

Using each of the temperature profiles in Figure 2, the plots of Figure 10 show a sensitivity of the depth-integrated brightness temperature to the depth averaged internal physical temperature. Two curves are shown in each panel of Figure 10; the gray curve allows the change from a frozen rock base to a water base as discussed previously (which occurs only for average physical temperatures greater than 240 K), while the black curve does not. The behavior of the emission for ice sheets with an average physical temperature greater than 240 K is notable by the corresponding decrease in Tb for the water-base case (such as experienced over Lake Vostok). Although there is good coupling of upwelling radiation for a glacier frozen to its base, the increase in reflectivity at the sub-glacial ice water boundary extinguishes much of the upwelling radiation, thereby resulting in a 0.5 K decrease in the 0.5 GHz brightness temperature observed at the surface. This difference hints at the possibility to use radiometry to identify spatial distributions of sub-glacial water provided that the measurement system is sensitive to the emission from depth. The sensitivity to this effect evidently depends on the ice thickness, surface accumulation rate, and the various terms which contribute to the modeled temperature profile. Consequently Figure 10 is but one realization of a suite of possible outcomes that are particularly sensitive to the selection of parameters in the temperature model. If, for instance, the accumulation rate is changed to 0.015 m/yr and the thermal diffusivity is changed to an unlikely 60 m^2/yr the resulting temperature profiles remain realistic but the difference in Tb between frozen and unfrozen beds may increase to more than 1 K.

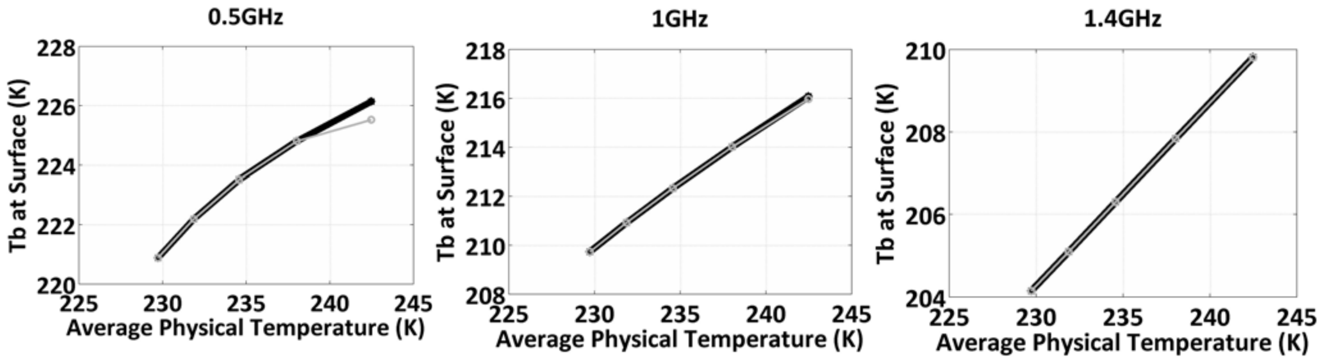

Figure 10. Estimated surface Tb versus average physical temperature for the loss models of Figure 3. The ice sheet base is wet for average temperatures of 240 K or more. The gray line represents the physical temperature models of Figure 2 and accounts for reflection-coefficient driven emission-reduction from the beneath the ice for subglacial water at 273 K (switching at above 240 K average physical temperature). The black line assumes the same physical temperature in the ice, but uses the same reflection coefficient for the rock and water case. This illustrates that both changing temperature profiles and changing bottom boundary conditions can modify the curves at the lowest frequency.

The brightness temperature values in Figure 10 are the sums of emission contributions from the sub-glacial layer and the ice sheet. Figures 11 examine these contributions separately for 0.5 GHz, where the sensitivity to basal properties is greatest. Figure 11 (left) shows the contribution at the surface from the sub-glacial layer. For the coldest ice sheet temperatures, the sub-glacial material contributes more than 60 K of the total 221 K signal. This effect decreases with increasing ice temperature and when water is allowed to form at the glacier base. Similarly, Figure 11 (right) shows the contribution of the ice sheet volume to the observed brightness temperature.

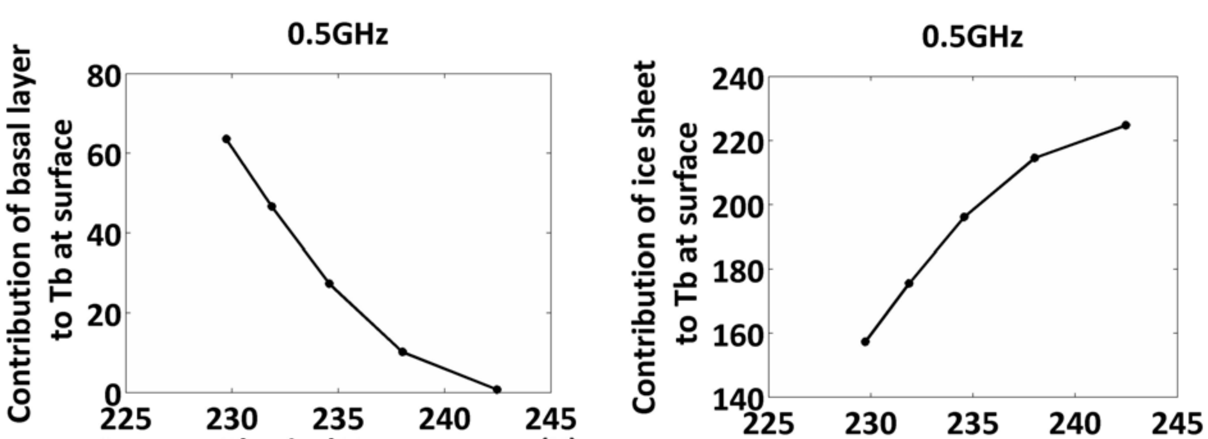

Figure 11. Contribution of the basal layer to the 0.5 GHz brightness temperature at the surface (left). Contribution of the ice sheet volume to the brightness temperature at the surface (right).

These results indicate brightness temperature sensitivity throughout the volume of the ice sheet at frequencies below 1 GHz. Above 1 GHz, the contributions from ice at depth become muted and near surface physical temperatures dominate the brightness temperature signal. In a separate analysis Drinkwater and others [22] estimate that at most, L-band sensitivity should persist only to around several hundred meters into the ice sheet at Dome C, Antarctica, though the sensitivity is acknowledged to be limited by the residual uncertainty in our present knowledge of temperature dependent absorption within the ice. Especially at lower frequencies, the modeling results here suggest the possibility for probing temperatures deep within the ice sheet. Meanwhile, multifrequency techniques could help to resolve ambiguities in the magnitude of the depth dependent losses, and thus the depth-dependent contribution to brightness temperature.

In the following section the L-band satellite microwave radiometer data are analyzed to quantify the observed variability in microwave brightness temperature in relation to known features such as Vostok sub-glacial lake.

3.0 SMOS Observations

The European Space Agency (ESA) Soil Moisture and Ocean Salinity (SMOS) satellite collects data suitable for preliminary comparison with our model results [23]. The satellite carries the Microwave Imaging Radiometer using Aperture Synthesis (MIRAS) which operates at 1.41 GHz [24]. The instrument is operated in a full polarization mode, so that horizontally and vertically polarized brightness temperatures are observed along with the third and forth Stokes parameters. The radiometric accuracy of SMOS observations varies across the swath, but is typically between 2 and 4 K [24]. The interferometric nature of the MIRAS instrument provides brightness temperature measurements at multiple observation angles (ranging from nadir up to 80 degrees incidence angle) during a single overpass; the specific set of incidence angles obtained depends on the location of the desired ground point within the SMOS swath. The SMOS spatial resolution also varies within the swath, but is typically in the range 33-50 km.

We investigate brightness temperature variations in the region around Vostok Station located in East Antarctica. Some 3700 m of ice separate the surface station from a sub-glacial lake which is several hundred meters deep and about the size of Lake Erie. The choice of location allows for investigating spatial changes in average physical temperature, ice physical properties, and changing basal conditions. The locations of SMOS brightness temperature measurements acquired over Lake Vostok are shown in Figure 12. In this study, we used SMOS Level 1c data obtained from the Operational Processor (L1OP) version V5.05. More than 350 SMOS L1c data were obtained and these spanned over two months from January to February 2012. The average bi-monthly brightness temperature values were resampled to a fixed grid (ISEA 4H9) with a spatial resolution between the nodes (also called DGG = Digital Global Grid) of about 15 km. The 1.4 GHz vertically and horizontally polarized SMOS data near 25^{o} and 55^{o} incidence angle are interpolated using an inverse distance weighting scheme (figure 13) and overlaid on a Radarsat C-band image mosaic with a polar stereographic projection [25]. The bright, radar regions extending away from the lake location are associated with higher backscattering from the ice divide where the accumulation rate is low. The location of the ice divide is correlated with cooler Tb values. However, note that the coldest brightness temperatures are observed within the known boundary of the lake [26, 27].

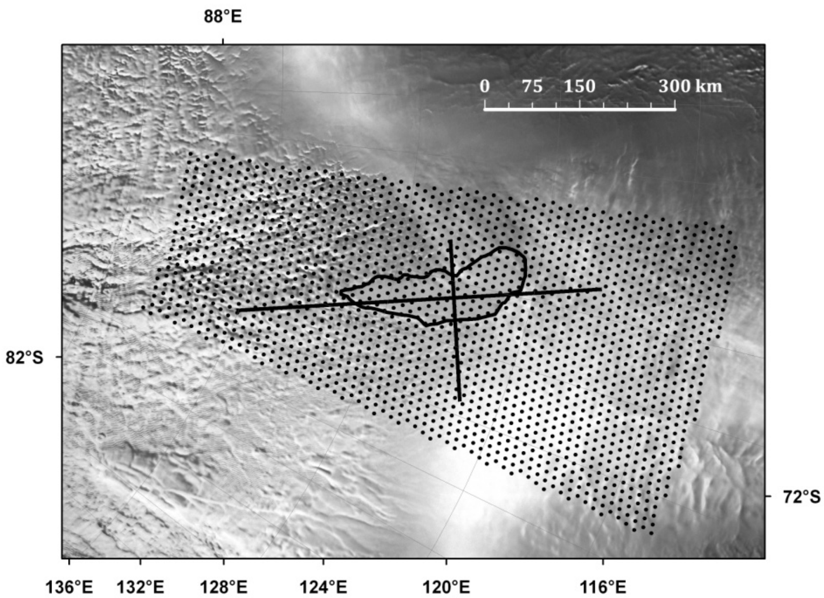

Figure 12. Locations (dots) of Level 1c SMOS brightness temperature measurements over Lake Vostok, Antarctica. The curved dark outline is the location of the lake as determined from the background Radarsat-1 SAR image. SMOS data are extracted along profile lines (straight black lines running roughly south to north and west to east) as discussed in Figures 14 and 15.

Figures 14 and 15 illustrate horizontally and vertically polarized brightness temperatures at 25^{o} and 55^{o} incidence angles that were extracted along the true, south-to-north and west-to-east lines shown in Figure 12. In the same figures the total ice thickness [28], is also shown along the transect. As expected, V-polarized brightness temperature data are warmer than H-polarized temperatures because of reflection coefficient differences. From the figures we observe that at low incidence angle the Tb anomaly for each transect is almost the same at V and H polarization and the Tb trend shows a good correlation with the ice thickness. The east west anomaly is about 5 K at 25° incidence angle and around 4.5 K at 55° incidence angle at both H and V polarization. The south north profiles trend perpendicular to the ice divide and so traverses changing glacial regimes. As a consequence the Tb anomaly is larger than in the previous case and reached more than 10 K for all incidence angle and polarization except for V polarization and 55° of incidence angle where it exhibits a value of 5 K. Near surface variability in scattering along the north south profile is evident from SAR imagery which consistently shows the ice divide to be a relatively stronger, more homogeneous scattering region than the surrounding parts of the ice sheet. The west/east line runs more nearly parallel to the ice divide and may be less susceptible to changes in surface physical properties such as firn density and grain size which change with distance from the divide. Consequently, we suggest that the 4-5 K Tb anomaly over the lake and along the west/east line which was observed by both polarization and both incidence angles better captures subsurface information and ice thickness differences. The 4-5 K temperature anomaly at the SMOS frequency is larger than we predict (less than 1K) for a transect running from a frozen to a liquid bed but it could also be explained by the difference in ice thickness (from around 2600 to around 4400 m which is mainly due to the bedrock relief) which in turn will modify the temperature profile.

These results are suggestive of a correlation between deep ice sheet physical temperatures and SMOS brightness temperatures. That said, we cannot rule out other potential spatially changing variables. In particular, changes in near surface layering as investigated by Drinkwater and others [22, their Figure 3] may also cause a spatial Tb anomaly over the lake. In the next section, we discuss a concept for more fully exploring the relationship between UHF emission and ice sheet physical properties, and in particular to investigate the potential for extracting physical temperature at various depths in the ice sheet.

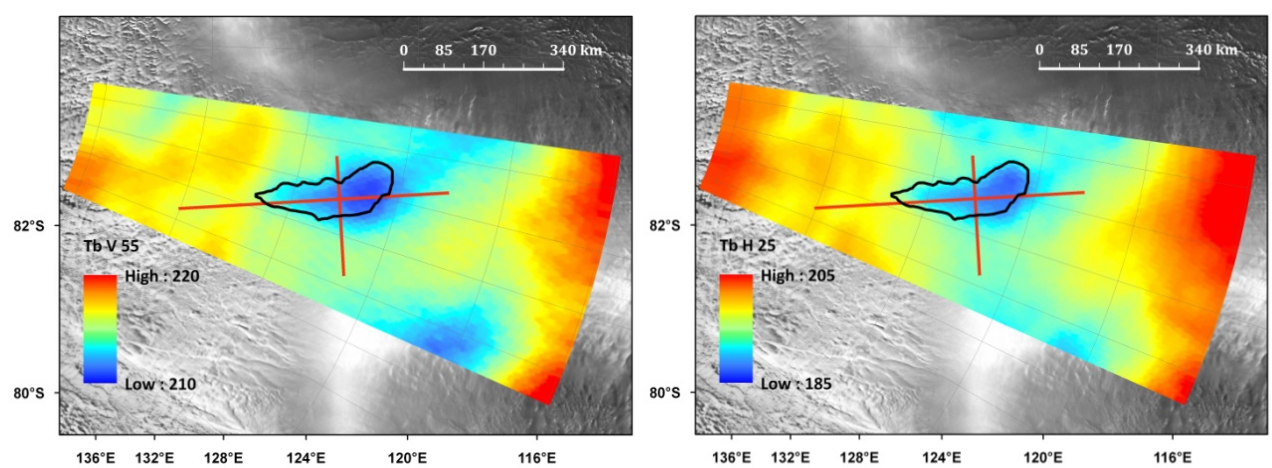

Figure 13. SMOS vertically polarized data at 55^{o} *incidence angle (left) and horizontally polarized data at* 25^{o} *incidence angle (right) over Lake Vostok (outlined in black). The data were collected in early 2012. There is a weak indication of a cold Tb anomaly correlated with the lake location. Red lines depict the locations where brightness temperature profiles were extracted (shown in Figures 14 and 15). The north-south transect runs from right to left whilst the east-west transect runs from top to bottom.*

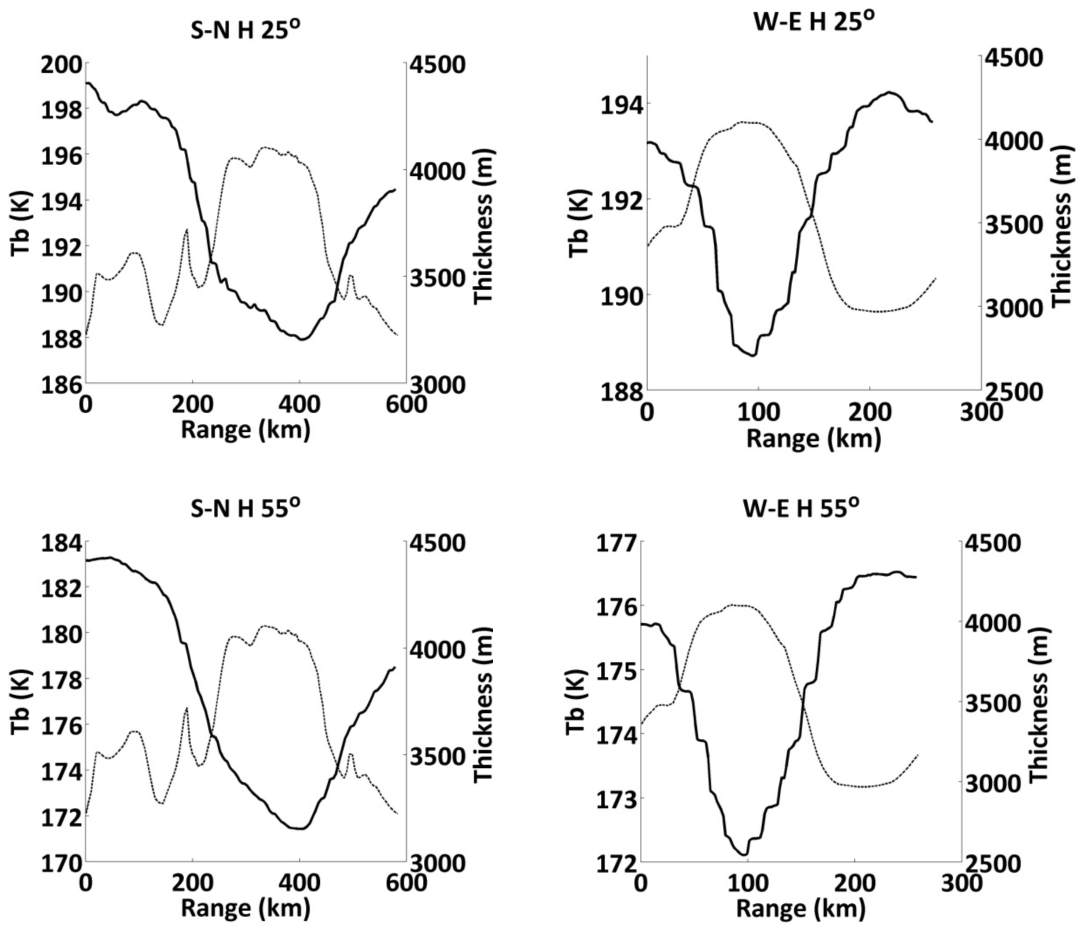

Figure 14. SMOS horizontally polarized brightness temperature data (heavy, black curves) along transects going from south to north (sn) (left panels) and west to east (we) (right panels) profiles shown in Figure 13. Data were selected at 25^o incidence angle (upper panels) and at 55^o incidence angle (lower panels). The intersection of the west to east and the south to north profiles (shown in Figure 13) occurs at about 320 km along the south to north profiles and about 90 km on the west to east profile. Ice thickness [28] is shown by the thinner, gray line.

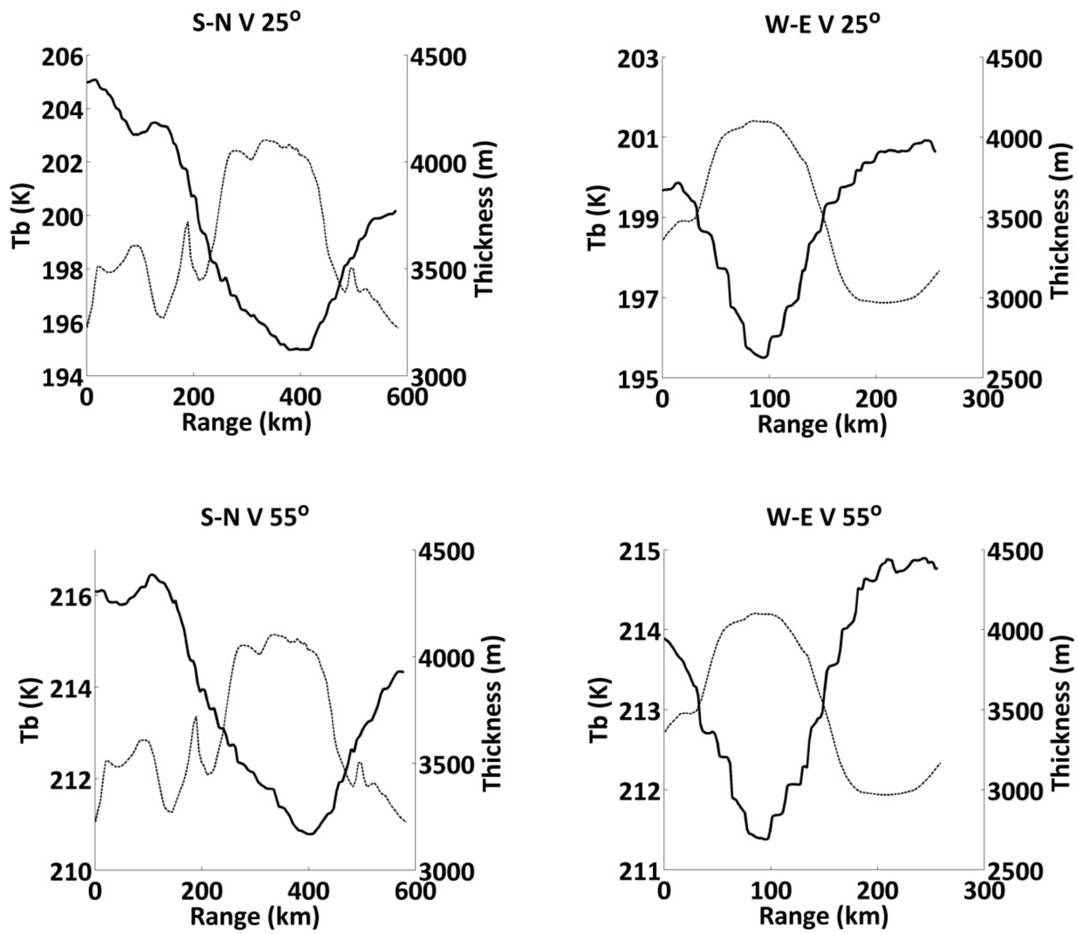

Figure 15. SMOS vertically polarized brightness temperature data (heavy, black curves) along transects going from south to north (sn) (left panels) and west to east (we) (right panels) shown in Figure 13. Data were selected at 25^o incidence angle (upper panels) and at 55^o incidence angle (lower panels). The intersection of the west to east and the south to north profiles in Figure 13 occurs at about 320 km along the south to north profiles and about 90 km on the west to east profiles. Ice thickness [28] is shown by the thinner gray line.

4.0 Conclusions: UltraWideBand Radiometry Concept

We modeled UHF brightness temperatures for thick polar ice and find that brightness temperature data are sensitive to relative changes in average ice sheet internal temperature at depth. For loss profiles consistent with the literature, we find that emission over the entire depth of the ice sheet can potentially contribute to the integrated signal at lower frequencies. Moreover we find that regions of frozen and unfrozen ice sheet base yield a signature associated with the changing electromagnetic boundary condition. Such information, whether it be from the upper tens of meters of the ice sheet or from the deepest regions, is crucial for improving glacier dynamics models.

To exploit this analysis and achieve a new glaciological measurement, we are developing the Ultrawideband Software-Defined Microwave Radiometer (UWBRAD) concept (Table 1). We envision the system will provide brightness temperature measurements in 15 channels from 0.5-2 GHz for ice sheet internal temperature sensing. The system will fully digitize the 1.5 GHz observational bandwidth, and will implement real-time detection and mitigation of radio frequency interference (RFI) in order to exploit all available unoccupied spectrum. The highly resolved frequency information to be obtained will also allow any evidence of strong internal reflection to be determined by searching for oscillations in observed brightness temperatures as a function of frequency. A novel ultrawideband antenna will also be constructed for the system to provide single polarization measurements at nadir from an airborne platform. The system will be designed for deployment on Twin Otter and possibly other aircraft. The objective is to use the multifrequency data to back out the temperature at depth in a manner similar to the approach used in sounding estimates of atmospheric temperatures [29, p. 1349]. Though initially focused on ice sheet applications, UWBRAD measurements would also be applicable to many other science applications where penetration into a transmissive medium is of interest, including deep subsurface or sub-forest canopy soil moisture information, sea-ice thickness sensing, and biomass observations.

The analyses presented have shown the sensitivity of brightness temperatures to internal ice sheet temperatures. Methods for retrieving temperature information from multichannel brightness temperature measurements are currently being developed, and will be reported in future work. Additional analyses of brightness temperature models are also progress to assess the current model utilized and to allow the impact of additional scattering or coherent layering effects in the ice sheet to be investigated.

Table 1

Freq (GHz)	0.5-2, 15 x 100 MHz channels
Polarization	Single (Right-hand circular)
Observation angle	Nadir
Spatial Resolution	1 km x 1 km
Integration time	100 msec
Ant Gain (dB) /Beamwidth	11 dB 30°

Calibration (Internal)	Reference load and Noise diode sources
Calibration (External)	Sky and Ocean Measurements
Noise equiv dT	0.4 K in 100 msec (each channel)
Interference Management	Full sampling of 100 MHz bandwidth in 16 bits resolution in each channel; real time “software defined” RFI detection and mitigation
Initial Data Rate	700 Megabytes per second (10% duty cycle)
Data Rate to Disk	<1 Megabyte per second

6.0 Acknowledgments

This work was partly supported by NASA’s Cryospheric Research and IIP Programs. SMOS datasets were provided by the European Space Agency.

7.0 References

[1] Jezek, K., 2012. Airborne and Spaceborne Remote Sensing of Cryosphere. In Encyclopedia of Sustainability Science and Technology, R.A. Meyers (ed.), vol 1., p. 280-298

[2] Nye, J. F., 1953. The flow law of ice from measurements in glacier tunnels, laboratory experiments, and the Jungfraufirn borehole experiment. Proc. Royal, Soc., Ser. A, vol 219, no 1139, p. 477-89.

[3] Glen, J. W., 1958, The flow law of ice. IAHS, publication 47, p. 171-183.

[4] Hooke, R., 1981. Flow law for polycrystalline ice in glaciers: Comparison of theoretical predictions, laboratory data and field measurements. Rev. Geophysics and Space Physics, vol. 19, no. 4, p. 664-672.

[5] Van der Veen, C. J., 1999. *Fundamentals of Glacier Dynamics.* Rotterdam: A. A. Balkema, 462 pp.

[6] Ritz, C., 1989. Interpretation of the temperature profile measured at Vostok, East Antarctica. Annals of Glac., vol. 12, p. 138-144.

[7] Salamatin, A. N., V.Y. Lipenkov, and K.V. Blinov, 1994. Vostok (Antarctica) climate record time-scale deduced from the analysis of a borehole-temperature profile, Ann. Glaciol., 20, p207–214.

[8] Thoma, M., K. Grosfeld, C. Mayer, and F. Pattyn, 2012. Ice-flow sensitivity to boundary processes: a coupled model study in the Vostok Subglacial Lake area, Antarctica, Ann. Glaciol. 53(60), p.173-180 doi:10.3189/2012AoG60A009.

[9] Johari, G.P., and P. A. Charette, 1975. The permittivity and attenuation in polycrystalline and single-crystal ice Ih at 35 and 60 MHz. J. Glac., vol 14, no 71, p. 293-303.

[10] Mätzler, C., 2006. Microwave dielectric properties of ice. In Thermal Microwave Radiation: Applications for Remote Sensing, eds. C. Mätzler, P. Rosenkranz, A. Battaglia, and J. Wigneron, IET Electromagnetic Waves Series, vol 52, Institute of Engineering and Technology, Stevenage, U.K., p. 455-462.

[11] Von Hippel, A., 1988. The dielectric relaxation spectra of water, ice and aqueous solutions and their interpretation; Part 3. IEEE Trans Electrical Insulation, vol 23, no. 5, p. 825-840.

[12] Evans, S., 1965. Dielectric properties of snow and ice – a review. J. Glac., vol. 5, p. 773-792.

[13] Hobbs, P., 1974. Ice Physics. Clarendon Press, Oxford, 837 p.

[14] MacGregor, J., K. Matsuoka, E. Waddington, D. Winebrenner, and F. Pattyn, 2012. Spatial variation of englacial radar attenuation: Modeling approach and application to the Vostok flowline. J. Geophs. Res., Vol. 117, F03022, doi:10.1029/2011JF002327.

[15] Hufford, G., 1991. A model for the complex permittivity of ice at frequencies below 1 THz. Int. J. Infrared and Millimeter Waves, vol 12, p. 677-682.

[16] Tsang, L., J. Kong and R.T. Shin, 1985. Theory of Microwave Remote Sensing, Willey Interscience, New York.

[17] Zwally, H. J., 1977, Microwave emissivity and accumulation rate of polar firn, *J.Glaciol.*, *18*(79).

[18] Swift, C.T., P.S. Hayes, J.S. Herd, W. L. Jones, and V.E. Delnore, 1985. Airborne microwave measurements of the Southern Greenland Ice Sheet. J. Geophys. Res: Solid Earth, vol 90, no B2, p. 1983-1994.

[19] Van der Veen, C.J. and K.C. Jezek, 1993. Seasonal variations in brightness temperature for Central Antarctica. *Annals of Glaciology*, 17, 300-306.

[20] Gow., A. J., 1971. Depth-time-temperature relationships of ice crystal growth in polar glaciers. CRREL Research Report 300, U.S.A. Cold Regesions Research and Engineering Laboratory, Hanover, NH, 23 p.

[21] Lipenkov, V.Y., A. Salamatin, and P. Duval. 1992. Bubbly-ice densification in ice sheets: II. Applications. J. Glac., vol 43, no 145, p. 397-407,

[22] Drinkwater, M., N. Floury, and M. Tedesco. 2004. L-band ice-sheet brightness temperatures at Dome C, Antarctica: spectral emission modeling, temporal stability and impact of the ionosphere. Annals of Glaciology, vol 39, p. 391-396.

[23] SMOS Special Issue, 2012. IEEE Trans Geoscience and Remote Sensing, Vol 50, no. 5.

[24] Kerr, Y.H., P. Waldteufel, J-P. Wigneron, F. Cabot, J. Boutin, M-J. Escorihuela, N. Reul, C. Gruhier, S. Juglea, J. Font, S. Delwart, M.R. Drinkwater, A. Hahne, M. Martin-Neira, and S. Mecklenburg, 2010. The SMOS mission: a new tool for monitoring key elements of the global water cycle, *Proc. IEEE*, Vol. 98(5), doi: 10.1109/JPROC.2010.2043032, pp. 666 – 687.

[25] Jezek, K, 2003. Observing the Antarctic Ice Sheet using the RADARSAT-1 Synthetic Aperture Radar. Polar Geography, vol 27, no. 3, p. 197-209.

[26] Jezek, K., J. Johnson, and M. Aksoy, 2012. Radiometric approach for estimating relative changes in intra-glacial average temperature. EOS Supplement, 2012 Fall AGU meeting.

[27] Brogioni, M., R. Rahmoune, and G. Macelloni, submitted. Characterization of the spatial and temporal stability of East-Antarctic plateau using SMOS data. IEEE TGRS.

[28] Fretwell, P. and 58 others. Bedmap2: improved ice bed, surface and thickness datasets for Antarctica. The Cryosphere, 7, 375-393, doi:10.5194/tc-7-375-2013, 2013

[29] Ulaby, F., R. Moore and A. Fung, 1986. Microwave Remote Sensing: Active and Passive: From Theory to Applicaitons. Vol. 3, Artech, Norwood, MA, 2162 p.